Solid Oxide Cell Reactor Model for Transient and Stationary Electrochemical H_2O and CO_2 Conversion Process Studies

Solid Oxide Cell Reactor Model for Transient and Stationary Electrochemical H₂O and CO₂ Conversion Process Studies

F. Sedeqi,[1,z] S. Santhanam,[1,2] M. Riegraf,[1] M. Riedel,[1] M. P. Heddrich,[1] and S. A. Ansar[1]

[1]*German Aerospace Center (DLR), Institute of Engineering Thermodynamics, Stuttgart, Baden-Württemberg 70569, Germany*
[2]*Shell Global Solutions International B.V., Amsterdam, North Holland 1031 HW, Netherlands*

The ability of high-temperature solid oxide cell (SOC) electrochemical reactors to efficiently convert atmospheric carbon to high value chemicals for industrial and energy storage applications via CO_2 and co-electrolysis makes them a key technology for active carbon utilisation. However, due to additional operational risks from thermochemical reactions on thermal management, limited experimental capacity, and relative novelty, CO_2 and co-electrolysis lag behind steam electrolysis in large-scale adoption. Here, a 1D+1D SOC model based on fundamental first principles considering three-dimensional heat transfer was improved via a unique method for representing co-electrolysis electrochemistry, solving with low computational effort. Validation against experimental data for two compositions and pressures, showed high levels of accuracy with respect to characteristic cell voltages, temperatures, and outlet compositions. The model also showed CO_2 reduction during co-electrolysis mainly occurred via reverse water gas shift, while CO_2 electrolysis still accounted for up to 35% of the total share. Pressurised co-electrolysis operation promotes exothermic methanation, causing pronounced heating of the reactor, consequently reducing the isothermal current density. Therefore, low to moderate pressurisation is likely most suited for coupling with downstream synthesis processes to avoid the installation of unnecessarily large systems and associated high costs.

Supplementary material for this article is available online

List of Symbols

Latin Symbols

A	Area, m^2
c	Specific Heat Capacity, $J/kg/K$
D_H	Hydraulic Diameter, m
$\mathscr{D}$	Mass Diffusivity, m^2/s
E_a	Activation Energy, J/mol
F	Faraday Constant, $96485\,C/mol$
g	Molar Specific Gibbs Energy, J/mol
h	Specific Enthalpy, J/kg
$\bar{h}$	Convective Heat Transfer Coefficient, $W/m^2/K$
j	Current Density, A/m^2
j_0	Exchange Current Density, A/m^2
l	Length, m
$\dot{m}$	Mass Flow, kg/s
M_j	Molar mass of component j, kg/mol
$\bar{N}$	Molar Flux, $mol/m^2/s$
Nu	Nusselt Number, $-$
p	Pressure, pa
$\dot{q}''$	Heat Flux, $J/m^2/s$
$\dot{Q}$	Heat Flow, J/s
$\dot{r}$	Reaction Rate, $mol/m^3/s$
R	universal Gas Constant, $8.314\,J/mol/K$
$\dot{R}$	Total Species Chemical Production, mol/s
R_{th}	Radiative Thermal Resistance, K/W
T	Temperature, K
u	Specific Internal Energy, J/kg
U_{op}	Voltage, V
U_N	Reversible Potential, V
x	Mass Fraction, $-$
y	Mole Fraction, $-$

Greek Symbols

α	Symmetric Factor, $-$
γ	Preexponential Factor for j_0, $A/m^2/K$
ϵ	Radiative Emissivity, $-$
η	Overpotential, V
λ	Conductive Heat Transfer Coefficient, $W/m/K$
ν	Reaction Stoichiometric Coefficient, $-$
ρ	Density, kg/m^3
σ	Boltzmann Constant, $5.67\,W/m^2/K^4$
ϕ	Porosity, $-$
ψ	Channel Factor, $+1$ for Fuel Channel, -1 for Air Channel

Subscripts

Act	Activation
Diff	Diffusion
H	H_2/H_2O Electrochemical Reaction
C	CO/CO_2. Electrochemical Reaction
A	Air side Electrochemical Reaction
k	Cell Number
j	Gas Species (i.e. O_2)
X0	Entering x-coordinate
X1	Leaving x-coordinate
Y0	Entering y-coordinate
Y1	leaving y-coordinate
Z0	Entering z-coordinate
Z1	leaving z-coordinate
cell	For the cell
i	Control Volume Number
cond	Conduction
rad	Radiation
conv	Convection
gas	Of gas mixture
EC	Electrochemical Reaction
x,y,z	Direction of flow
reac	Reactant in electrochemical reaction
prod	Product in electrochemical reaction
α	Main Species of consideration in multicomponent diffusion

zE-mail: faisal.sedeqi@dlr.de

β	Other existing species in multicomponent diffusion
α'	Corresponding species in electrochemical reaction for multicomponent diffusion
Ω	Ohmic

Superscripts

eff	effective
TPB	At the TPB
WGS	WGS reaction
MSR	MSR reaction
H	H_2/H_2O Electrochemical Reaction
C	CO/CO_2 Electrochemical Reaction
A	Air side Electrochemical Reaction

With the ambitious targets set by international organisations to reduce carbon emissions through fossil fuel consumption, development of renewable intermittent technology has grown substantially.[1] Furthermore, with lower fossil fuel consumption and growing demand for electricity, new methods of producing traditionally fossil fuel derived products are required, using the growing electricity supply. High temperature planar solid oxide cell (SOC) reactors have been regarded as a key technology to achieve these goals efficiently.[2] Operating at temperatures ranging 650 °C–900 °C, they can not only produce electricity and heat under fuel cell operation very efficiently, but also convert electricity in the form of fuel and commodity chemicals such as hydrogen and carbon monoxide through electrolysis of steam and carbon dioxide (CO_2), respectively. Furthermore, SOCs can directly produce syngas through the co-electrolysis (coEl) of steam and CO_2,[3] facilitating the production of numerous valuable chemicals in a sustainable and carbon-neutral manner. In this respect, they can be integrated in such process systems to continuously produce the same products efficiently and cleanly.

Usage of SOCs for energy storage and industrial applications is maturing and currently rapid scaleup of production is occurring, with commercial units available today.[4] Nevertheless, despite the high potential of co-electrolysis, its adoption and understanding still lags behind steam electrolysis.[5] This is evident in the scale of projects and utilisation of SOC technology, an example of this is depicted in,[6] where the largest steam electrolysis demonstrator to date, with a size of $720kW_{AC}$, was integrated into a wider process, while the largest co-electrolysis installation currently has a smaller size of 220 kW. This is largely due to the added complexity from the occurrence of electrochemical reactions (Eqs. 1, 2), the thermochemical reactions of reverse/water gas shift (R/WGS) (Eq. 3) and methanation/steam reforming (M/SR) (Eq. 4) within the cells due to the existence of Ni catalytic materials, as well as the potential for carbon formation. These reactions bring additional thermal phenomena, as implied by the magnitude and sign of their reaction enthalpies. This complicates the controllability of the SOC reactors and increases the susceptibility to compounding thermal stress from the variations in thermal expansion between the different layers of the cell, leading to cell or stack failure.[7] Coupling this with the limited experimental capabilities, research into CO_2 and coEl is still mainly limited to well-known safe operation points. Furthermore, wider system relevant operating points such as elevated pressures for synergies with downstream synthesis processes, have only recently grown in interest. Having a better understanding of these complex phenomena through modelling will promote wide scale adoption of this technology by finding optimal operating points in wider operation scopes.

$$H_2 + 0.5O_2 \rightleftharpoons H_2O, \ \Delta_r H(800 \text{ °C}) = -248 \text{ kJ mol}^{-1} \quad [1]$$

$$CO + 0.5O_2 \rightleftharpoons CO_2, \ \Delta_r H(800 \text{ °C}) = -282 \text{ kJ mol}^{-1} \quad [2]$$

$$CO + H_2O \rightleftharpoons CO_2 + H_2, \ \Delta_r H(800 \text{ °C}) = -34 \text{ kJ mol}^{-1} \quad [3]$$

$$CH_4 + H_2O \rightleftharpoons CO + 3H_2, \ \Delta_r H(800 \text{ °C}) = 225 \text{ kJ mol}^{-1} \quad [4]$$
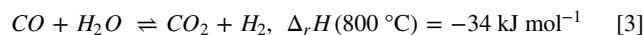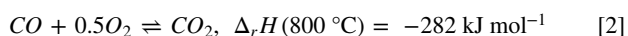
To adequately grasp the performance of SOC based systems, a computationally efficient model that accounts for the various electrochemical and transport phenomena between and around the stack is beneficial, especially to capture the heat transfer processes occurring within. These models can come in various resolutions from 0D to 3D. Most system level studies use 0D models of stacks or modules that do not consider the various transport phenomena within the cells and treat the SOC as a black box.[8] While these models are suitable for general plant conceptual design and sizing matters, they are unsuited in determining safe and optimal operating strategies, as the low resolution ignores internal thermal phenomena such as development of hot and cold spots that can have detrimental effects to the lifetime of the reactor.[7,9,10] The majority of stack level modelling utilise 1D models of cells discretised in the flow direction as they consider cells with regular geometries.[11,12] 2D cell models that discretise in the flow plane and perpendicular cell plane, are used for cells that have complex geometries resulting in irregular flow patterns.[13] As the cells and sublayers in the cells are very thin compared to their length and width, discretising in the vertical plane is mainly done to analyse local mass transfer phenomena and kinetics, and is usually not of interest at system level due to the higher computational effort, hence 2D cell models in this plane and 3D models in general are rarely used.[14] These cell models can be vertically stacked to model SOC stacks with cells that interact with each other and the surrounding environment, thereby adding another dimension to the model, with 1D cells, such a stack model would be 1D +1D. Further scaling/numbering up to model larger SOC modules that may interact with their surroundings will then make them relevant for the developing operating strategies for larger process applications.[15]

Most SOC models considering coEl, assume that the main pathway for the consumption of carbon dioxide is through the reverse water gas shift reaction,[16] due to the high operating temperature bringing the RWGS reaction to equilibrium. A model considering the electrochemical reaction kinetics can be used to determine the veracity of this claim and determine the extent of CO_2 electrolysis. Aicart et al.[17] introduced a parallel circuit model where each electrochemical reaction occurs at a portion of the available electrochemically active area normalised to the relative proportion of each reactant species which was also used by Banerjee et al.[11] who included detailed reaction micro-kinetics for the thermochemical reactions. Although this model of co-electrolysis behaviour is relatively simple to apply, it does not fully represent the physics of the process as it splits the cell into two sections where each electrochemical reaction occurs without interacting with the other. This essentially assumes the existence of two ionic currents within the cell and each fuel side electrochemical reaction influencing the air side. Bessler et al.[18] proposed that a local potential equilibrium occurs at the electrode-electrolyte interface where most of the charge transport reactions occur. This approach would only consider a parallel circuit at the fuel channel, and the rest of the cell as a series circuit. This approach is just as easy to implement, while holding physical relevance.

For these reasons mentioned, a previously developed 1D +1D SOC reactor model within the TEMPEST framework of the German Aerospace Center (DLR)[19] was updated to consider these effects for a 10-cell short stack. The framework is implemented in the object-oriented Modelica language[20,21] and executed through the commercial Dymola software.[22] The model as illustrated in Fig. 1, focusses on the electrochemically active part of the cell, hereby referenced as
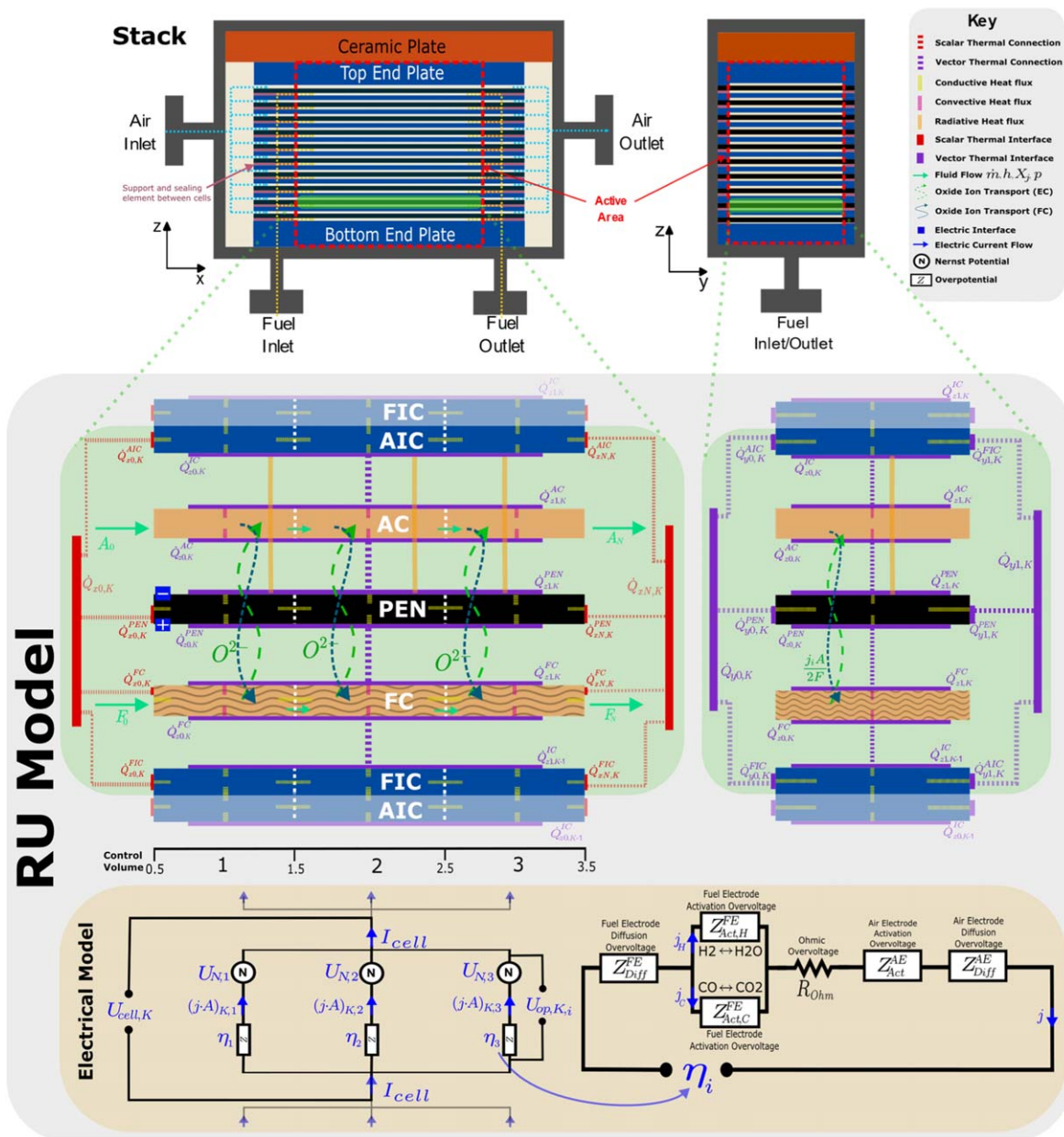
Figure 1. Schematic of the 1D+1D reactor model illustrating the heat and mass transport phenomena and interactions considered within and between the layers of an RU's active area with 3 control volumes (centre left for X-Z plane and right for Y-Z plane) in the context of a 10-cell SOC reactor (top). The electric circuit model (bottom) is also illustrated with a branch for the three control volumes as well as highlighting the cell resistance model (bottom right).

the active area. The passive area, denoting the section around the active area in the cell that does not accommodate the electrochemical reaction; but gives the multi-layered SOC reactor mechanical stability, current collection for the reactor, and pre-heats incoming fluids is not considered here. Work on the passive area as well as usage of this framework in larger SOC reactor modules for transient operation has been done by Tomberg et al.[23] (also relevant[15]). The model is capable of both fuel cell, electrolysis and reversible operation, but focus will be put especially on coEl operation. This work outlines the development process of the update to consider additional phenomena such as coEl and external heat transfer, as well as the validation procedure. Furthermore, the capability of the model to simulate different applications for SOC reactors outside of those validated is also investigated.

Model Description: 1D +1D SOC Reactor Model

This section outlines the model and the steps taken to modify the SOC model previously presented by Srikanth et al.[19] to consider the additional phenomena arising from coEl. Modifications were also made to the numerical structure to improve the solving performance. Furthermore, the heat transfer from the reactor to the surroundings was also modelled for a 10-cell SOC reactor in a pressurised furnace environment and validated against experimental measurements.

Numerical structure update.—The SOC reactor model was composed of vertically (z-axis) stacked repeat units (RU) or cells. As illustrated in Fig. 1, each RU is composed of five one-dimensional layers, discretised along the flow direction (x-axis).

The layers are arranged vertically in the form: interconnect (IC); fuel channel (FC); positive electrode-electrolyte-negative electrode (PEN); air channel (AC); and interconnect. To promote repeatability, ICs of half thickness were used in RUs, forming a complete IC when vertically stacked. Each half is then labelled based on the closest channel i.e. the fuel side IC (FIC) is directly interacting with the FC and the air side IC (AIC) directly interacts with the AC. The previous model presented by Srikanth et al.[19] considered each control volume (CV) within the layers as separate piecewise constant units comparable with multiple CSTRs in series, or upwind differencing. The update presented here treats each layer as one object analogous to a plug flow reactor, which allows for different discretisation methods including the first order upwind differencing used previously, as well as higher order schemes which can improve the model accuracy and stability with fewer CVs and thereby improve solving performance.

RU model.—All the layers have conservation equations of the form,

$$\frac{\partial b}{\partial t} = \frac{\partial}{\partial V}f(b) + \dot{s}(b) \qquad [5]$$

And when integrated over the 1D control volume it becomes,

$$\Delta x_i A \frac{d\bar{b}_i}{dt} = F_{i-\frac{1}{2}}A - F_{i+\frac{1}{2}}A + \dot{S}_i \qquad [6]$$

Where $\bar{b}_i$ denotes the averaged state property in a CV i, F denotes the flux entering and leaving as a function of the state at the interface, $\dot{S}$ denotes the sources and sinks. The layers vary in the phenomena they consider and therefore the fluxes and source terms differ. Hence, the 5 layers can be reduced to 3 model types: IC, flow channel and PEN. The IC only considers heat flows, the flow channels consider reactive gas thermohydraulic flows with mass transfer through the boundary, and the PEN considers thermal and electric flows with electrochemical reactions. Electricity flow in the IC is considered in the PEN model as an additional resistance. Each layer is modelled in a self-contained form, where interfaces define the boundary conditions and can be connected to other layers' interfaces to define equality points. Table I outlines the main equations used in the model depicted in Fig. 1.

The gas flow channels are modelled with a constant cross-sectional area, filled with porous nickel foam in the FC and fully void in the AC. It is generally assumed that the mass flux in the flow direction is predominantly convective, although diffusion may be important at lower flow speeds.[24] An additional mass flux, proportional to the current density, exists in the direction of the PEN (z-direction) due to the electrochemical reaction transporting oxide ions from one channel to the other. The existence of thermochemical reactions would further result in variations in composition and is accounted for in the species mass balance. The foam also impacts the heat transfer behaviour as it improves the conductive heat flux in the x-direction. The gas was assumed to be in thermal equilibrium with the foam, and the energy balance was performed with the gas and solid as a homogenous phase. The convective heat transfer rate between the solid surfaces of the PEN and IC surrounding the FC and AC was determined through the Nusselt number, Nu. By assuming steady flow between wide flat plates for the hydraulic diameter as was done in[25,26] and implementing the boundary conditions provided by the interfaces, for the porous foam filled FC constant Nusselt numbers of Nu = 12 and Nu = 9.86 for the PEN side and IC side, respectively, were given.[27] The constant Nu

implies that the structure and porosity, do not influence the convective heat transfer, however, to ensure fast simulation performance this constant value was used, especially since at the reactor level, the conductive heat transfer in the solid masses plays a more significant role. For the void AC Nu = 8.235 and Nu = 7.54 were used for the PEN and IC sides, respectively. This lack of foam in the AC also allowed for radiative heat transfer between the PEN and IC.

The IC was modelled as heat transfer through a solid, with the flux described by Fourier's law in the x-direction. There is additional heat transfer from the y- and z- axis through contact with the other layers and these are part of the source terms. Finite difference approximation of the spatial derivative term was used to account for the y- and z- boundary heat transfer.

The PEN lumps the fuel electrode (FE), electrolyte (EL) and air electrode (AE) into one object. As it is primarily solid, it has the same modelling skeleton of the IC model. However, additional source terms considering electrochemical phenomena, are additionally applied. These include, the heat of reaction from the electrochemical reaction at the TPB, and the electrical work input. This therefore requires the calculation of the cell voltage. As illustrated in the electrical model in Fig. 1, in the SOC, the voltage can be modelled as the sum of the reversible/Nernst voltage and the losses, which are composed of activation, ohmic, and diffusion overpotentials - these are detailed further below for coEl.

Finite volume implementation.—The model only stores the control volume averages and does not know the value at the interfaces i.e. at point $i - \frac{1}{2}$. Therefore, flux functions to relate to stored values must be specified to ensure the system of equations can be solved. For the diffusive fluxes e.g. conductive heat transfer, the central difference scheme was implemented which can be expressed as,

$$\dot{q}''_{IC,cond,i-\frac{1}{2}} = \lambda_{IC}\frac{\partial T_{IC}}{\partial x}\Big|_{i-\frac{1}{2}} \approx \lambda_{IC}\frac{(T_i - T_{i-1})}{\Delta x_i} \qquad [7]$$

For the convective fluxes e.g. species mass flow, numerous flux functions may be implemented. For reasons of stability and speed, the upwind difference scheme was used, as depicted in Eq. 8.

$$y_j\dot{m}|_{K,i+\frac{1}{2}} \approx y_j\dot{m}|_{K,i} \qquad [8]$$

This is numerically equivalent to the previous model, but now model has added flexibility to integrate other flux schemes for improved accuracy and/or stability. Future publications may consider the implementation of different schemes into the model.

Co-electrolysis model.—With the consideration of co-electrolysis, two electrochemical reactions at the FE (half reactions of Eqs. 1 and 2) occur. The rates of these electrochemical reactions can be represented through a current density for each corresponding reaction. This addition of an extra current density for the CO_2 electrolysis may alter the species composition in the FC, as a possible additional path for CO_2 reduction is considered compared to the previous case which ignored this path. The adjustment, by including the additional rate of reaction as a function of current density, is depicted in Table I.

The impact on the cell voltage calculation however, is more complicated, affecting the ideal voltage and FE overpotentials. Due to the nature of membrane electrochemical reactors such as SOCs, it was assumed that the polarisation effects of coEl are isolated to the fuel side and the air side electrochemical models were unchanged. The following section will outline the changes made to account for

Table I. Table of conservative equations and main constitutive equations used in new cell model depicted for internal control volume *i*.

Interconnect Energy Balance	$l_y l_{IC,z}\left((\rho c)_{IC}\frac{dT_{IC,i}}{dt} + \frac{1}{\Delta x_i}(\dot{q}''_{IC,cond,i-0.5} - \dot{q}''_{IC,cond,i+0.5})\right) = (\dot{q}''_{IC,z0} + \dot{q}''_{IC,z1})_i l_y + (\dot{q}''_{IC,y0} + \dot{q}''_{IC,y1})_i l_{IC,z} + \dot{q}_{rad\,IC,i} l_y$
Total Mass Flow in Gas Channel	$A_K \phi_K \frac{d\rho_{K,i}}{dt} = (\dot{m}_{K,i-0.5} - \dot{m}_{K,i+0.5})\cdot\frac{1}{\Delta x_i} + \psi_K\frac{j_i}{4F}\cdot l_y \cdot M_{O_2}, \ K \in \{AC,\ FC\}$
Species Mass Balance in Gas Channel	$\Delta x_i \cdot A_K \phi_K \cdot \frac{d(y_{j,i}\rho_{K,i})}{dt} = y_j\dot{m}|_{K,i-0.5} - y_j\dot{m}|_{K,i+0.5} + M_j \cdot \dot{R}_{K,j,i}, \ K \in \{AC, FC\}$
Fuel Channel Energy Balance	$\Delta x_i \cdot A_{FC}\left(\phi_{FC}\frac{d(\rho_{FC,i}\cdot u_{FC,i})}{dt} + (1 - \phi_{FC})\cdot\rho_{Ni}c_{Ni}\frac{dT_{FC,i}}{dt}\right) - \dot{m}h|_{FC,i-0.5} + \dot{m}h|_{FC,i+0.5}$
	$= \dot{Q}_{FC,conv,z0} + \dot{Q}_{FC,conv,z1} + \left(\frac{j_{H,i}}{2F}(h_{H_2O} - h_{H_2}) + \frac{j_{C,i}}{2F}(h_{CO_2} - h_{CO})\right)\Delta x_i l_y - l_y l_{FC,z}(\dot{q}''_{FC,cond,i-0.5} - \dot{q}''_{FC,cond,i+0.5})$
Air Channel Energy balance	$\Delta x_i A_{AC}\frac{d(\rho_{AC,i}\cdot u_{AC,i})}{dt} = \dot{m}h|_{AC,i-0.5} - \dot{m}h|_{AC,i+0.5} + \dot{Q}_{AC,z0} + \dot{Q}_{AC,z1} - \frac{j_i}{2F}(0.5h_{O_2})\Delta x_i l_y$
Convective Heat Transfer Rate	$\dot{Q}_{K,conv,z,i} = \bar{h}_{K,i}A(T_{K,i} - T_{s,z,i}), \ K \in \{AC, FC\}$
Convective Heat Transfer Coefficient	$\bar{h} = Nu\cdot\frac{\lambda_{gas}}{D_H}$
Conductive Heat Flux	$\dot{q}''_{K,cond,i+0.5} = \lambda_K\left(\frac{T_{K,i} - T_{K,i+1}}{\Delta x}\right), \ K \in \{IC, PEN, FC\}$
Pressure Drop	$\dot{m}_{FC,i-\frac{1}{2}} = \rho_{FC,i-\frac{1}{2}}\cdot\left(\frac{l_y\cdot l_{FC,z}^3}{12\mu_{FC}}\right)\cdot\left(\frac{p_{FC,i-0.5} - p_{FC,i}}{\Delta x_i}\right)$
PEN Energy Balance	$l_y l_{PEN,z}\left((\rho c)_{PEN}\frac{dT_{PEN,i}}{dt} + \frac{1}{\Delta x_i}(\dot{q}''_{PEN,cond,i-0.5} - \dot{q}''_{PEN,cond,i+0.5})\right)$
	$= (\dot{q}''_{z0} + \dot{q}''_{z1})_{PEN,i}\Delta x_i l_y + (\dot{q}''_{y0} + \dot{q}''_{y1})_{PEN,i}\Delta x_i l_{PEN,z} + \Delta x_i l_y\cdot(jU_{op} + \dot{q}''_{EC} + \dot{q}''_{rad\,PEN})_i$
Voltage Balance	$U_{op,i} = U_{N,i} - j_i ASR_{\Omega,i} - \eta_{Act,FE,i} - \eta_{diff,FE,i} - \eta_{Act,AE,i} - \eta_{diff,AE,i}$
Heat of Reaction	$\dot{q}''_{EC,i} = \frac{j_{H,i}}{2F}\Delta_r H_{H,i}(T_{PEN,i}) + \frac{j_{C,i}}{2F}\Delta_r H_{C,i}(T_{PEN,i})$
Fuel Side Reaction Rate	$\dot{R}_{j,i} = \left((\nu_j^{WGS}\dot{r}_i^{WGS} + \nu_j^{MSR}\dot{r}_i^{MSR})l_{FC,z} + \nu_j^H\frac{j_{H,i}}{2F} + \nu_j^C\frac{j_{C,i}}{2F}\right)\Delta x_i l_y$
Co-electrolysis current relation	$j_i = j_{H,i} + j_{C,i}$
Air Side Reaction Rate	$\dot{R}_{j,i} = \nu_j^A\frac{j_i}{2F}\Delta x_i l_y$
Ideal Gas Law	$p_i M_i = \rho_i R T_i$
KVL	$U_{op,cell} = U_{op,i}$
KCL	$I_{cell} = l_y\sum\Delta x_i j_i$
BVE for H-Reaction	$j_{H,i} = j_{0,H,i}\left[\exp\left(\alpha_H\cdot\frac{2F\eta_{Act,H,i}}{RT_{PEN,i}}\right) - \exp\left(-(1 - \alpha_H)\cdot\frac{2F\eta_{act,H,i}}{RT_{PEN,i}}\right)\right]$
BVE for C-Reaction	$\eta_{Act,C,i} = \frac{RT_{PEN,i}}{F}\sinh^{-1}\frac{j_{C,i}}{2j_{0,C,i}}$
BVE for AE	$j = j_{0,A}\cdot\left[\exp\left(\alpha_A\cdot\frac{2F\eta_{act,A}}{RT_{PEN}}\right) - \exp\left(-(1 - \alpha_A)\cdot\frac{2F\eta_{act,A}}{RT_{PEN}}\right)\right]$
FE Diffusion Overpotential	$\eta_{diff,FE,i} = -\frac{RT_{PEN,i}}{4F}\ln\left(\frac{y_{H_2O,i}\cdot y_{CO_2,i}\cdot y_{H_2,i}^{TPB}\cdot y_{CO,i}^{TPB}}{y_{H_2,i}\cdot y_{CO,i}\cdot y_{H_2O,i}^{TPB}\cdot y_{CO_2,i}^{TPB}}\right)$
AE Diffusion Overpotential	$\eta_{diff,AE,i} = -\frac{RT_{PEN,i}}{4F}\ln\left(\frac{y_{O_2,i}^{TPB}}{y_{O_2,i}}\right)$

coEl operation, as illustrated in the electric circuit model depicted in Fig. 1. The equations can easily be adjusted to consider steam or CO_2 only electrochemical reactions.

Ideal voltage.—For the ideal voltage, several approaches may be considered such as using only one of the two reactions or using the equilibrium oxygen compositions or even implementing the mixed potentials.[28] However, they all have their drawbacks in terms of accuracy, ease of implementation or performance. Here the global coEl reaction (Eq. 9) was used to calculate the ideal voltage with the

Nernst equation (Eq. 10) with the averaged CV values. This approach has the benefit of flexibly handling concentration variations in coEl mixtures, especially along the length of the reactor.

$$CO + H_2 + O_2 \rightleftharpoons H_2O + CO_2 \qquad [9]$$
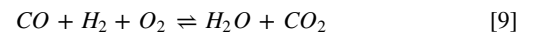
$$U_{N,i} = -\frac{\Delta g^\circ(T_i)}{4F} - \frac{RT_i}{4F}\ln\frac{p_{H_2O,i}p_{CO_2,i}}{p_{H_2,i}p_{CO,i}p_{O_2,i}} \qquad [10]$$

Activation overpotential.—The modelled electrolyte supported cells employed a LSCF/CGO air electrode and a Ni/CGO fuel electrode. To describe their electrochemical performance, the implicit form of the BVE for the three electrochemical reactions in the RU was used. The exchange current densities were defined in the form of Eq. 11, where p denotes the partial pressure of reactant and product gas species in each half reaction.

$$j_0 = \gamma T_{PEN} \cdot \left(\frac{p_{Reac, TPB}}{p_0} \right)^a \cdot \left(\frac{p_{prod, TPB}}{p_0} \right)^b \cdot \exp\left(-\frac{E_a}{RT_{PEN}} \right) \quad [11]$$

The parameters for the H_2/H_2O electrochemical reaction on Ni/CGO were determined experimentally,[3,29] along with the activation and pre-exponential factor for the CO/CO_2 reaction[29] by means of electrochemical impedance spectroscopy (EIS) and equivalent circuit modelling similar to the method described by Leonide et al.[30–32] In the stack EIS measurements, three major polarization resistance contributions were identified and their origin was in detail discussed elsewhere.[29] The processes were modelled by 3RQ elements and results are shown in Table II. It has been reported that the Ni/CGO fuel electrode impedance generally consists of a dominating surface process at frequencies of ~10 Hz which is referred to as the fuel electrode process in the present work, and a smaller bulk contribution at frequencies ~200 Hz.[33] Since the fuel electrode bulk process overlaps with the LSCF/CGO air electrode process, their resistance contributions could not be separated and they were described with a lumped process referred to as the air electrode process.

The determined parameters for the activation energy barriers and partial pressure dependencies deviate from the ones determined on cells for the same SOC technology.[35,36] However, in the cited publications the resistances were determined in symmetrical cell measurements and therefore, the fuel electrode resistance included both the surface and the bulk process which is in contrast to the lumped approach as described above.

According to Bessler et al.,[18] charge transfer reactions at the electrode/electrolyte interface are at a local equilibrium, and an equal potential is observed at this interface. Therefore in a given control volume, the H_2/H_2O and CO/CO_2 charge transfer reactions at the electrode surface during coEl exhibit equivalent activation overpotentials, expressed via Eq. 12 and the parallel circuit in Fig. 1. This competitively couples the two reactions kinetically, through the exchange current density. Further competition is provided by diffusion through the porous electrode discussed in the next section.

$$\eta_{Act,FE} = \eta_{Act,H} = \eta_{Act,C} \quad [12]$$

Table II. Electrochemical kinetic parameters with sources, for reproducing results.

Parameter	Value	Source
$E_{a,AE}$	106810 J mol^{-1}	Experiments in[34]
γ_{AE}	2.44×10^6 A m^{-2}	
a_{O_2}	0.298	
α_{AE}	0.5	
$E_{a,FE,H}$	95160 J mol^{-1}	Experiments in[34]
$\gamma_{FE,H}$	1.52×10^5 A m^{-2}	
a_H	0.04	
b_H	0.18	
$\alpha_{FE,H}$	0.5	
$E_{a,FE,C}$	125104 J mol^{-1}	Experiments in[34]
$\gamma_{FE,C}$	6.63×10^5 A m^{-2}	
$\alpha_{FE,C}$	0.5	
a_C	0.04	—
b_C	0.18	—

Diffusion overpotential.—In the model presented in,[37] the diffusion of the gas species through the porous electrodes between the channel and the triple phase boundary (TPB) reaction site, was modelled using an extended Fick's law model for ternary gas components. This was replaced by a multi-component gas diffusion model based on the Dusty Gas Model (DGM) as it has shown to be accurate in representing the mass diffusion process for multi-component gas diffusion through a porous structure. An analytical form of the DGM proposed by Fu et al.[38] was utilised here, as the DGM is an implicit equation and therefore computationally expensive for transient simulations.[39] The analytical solution was derived assuming constant pressure ($dp/dz = 0$) through the porous electrode resulting in Eq. 13.

$$-\frac{p}{RT} \cdot \frac{dx_\alpha}{dz} = \frac{\bar{N}_{z,\alpha}}{\mathscr{D}^{eff}_{K,\alpha}} + \sum_{\beta \neq \alpha} \frac{x_\beta \bar{N}_{z,\alpha} - x_\alpha \bar{N}_{z,\beta}}{\mathscr{D}^{eff}_{\alpha,\beta}} \quad [13]$$

Where the subscripts α and β denotes the species in question and the remaining species, respectively. This approach uses a combination of the Knudsen diffusion coefficient, $D^{eff}_{K,\alpha}$, defined by the kinetic theory of gases and binary molecular diffusion coefficient, $D^{eff}_{\alpha,\beta}$, obtained using the Chapman-Enskog theory based on the Lennard-Jones potential from the Wolfram tool,[40] example implementation of this can be found in the supplementary information. Both effective diffusion coefficients were calculated by considering the effect of electrode porosity and tortuosity which can be found in.[41] The molar flux, $\bar{N}_z$ through the porous electrode was defined in two ways. For the electrochemically active species (i.e. those involved in the electrochemical reactions), it was described by Faraday's law and proportional to the corresponding current density, while for the inactive species it was zero. On the fuel side, for electrochemically inactive species, Eq. 13 can be evaluated analytically, however for the electrochemically active species this is not easily possible due to the existence of two electrochemical reactions and therefore was evaluated numerically via finite difference method. For the air side, since only one electrochemical reaction occurs Eq. 13 can be evaluated analytically. The derivation is provided in the supplementary information.

Reactor model.—The SOC reactor model was developed based on the commercially available planar design SOC reactor as used in,[9] where several RUs are stacked on top of each other and closed off with thick end plates at the top and bottom of the stack. A ceramic plate is also placed on top to distribute pressure and provide gas tightness. Each RU interacts with its adjacent units and the surroundings of stack through three kinds of flows: gas flow, heat flow and electric flow. For the electric flow, the vertical stacking meant that the RUs were connected in series electrically and within the RU, each control volume was connected in parallel resulting in a uniform voltage throughout the RU.

Flow distribution in the reactor.—Flow distribution was important to consider as it could impact the reaction rates and voltages due to the varying residence times in each channel and therefore could affect local thermal behaviour. Here, uniform mass flow was assumed to all cells and the pressure drop along the channel which varies with local temperature, fluid density, channel geometry, and friction factor, was included through a steady momentum balance. Where, the pressure drop was defined through Darcy's law with the hydraulic diameter being calculated with the assumption of flow between two wide flat plates.

Heat transport in the reactor.—Heat transport within the reactor is critical as it affects the reactor performance, hence heat transport in both the active and passive area should be considered. For this study, the passive area was modelled as a lumped resistance between the active area and surroundings, and its influence on the entering
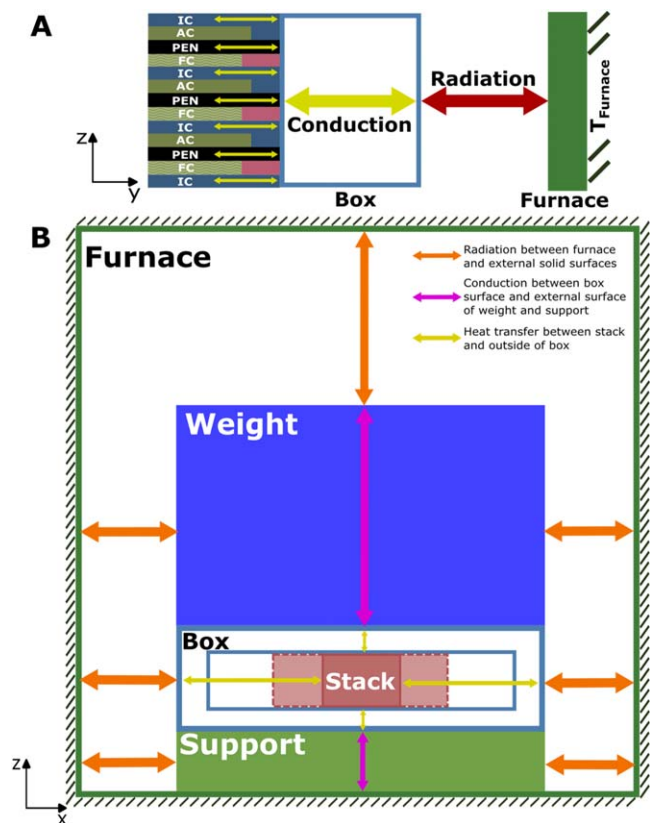
Figure 2. (A) Heat transfer between the SOC reactor and surroundings along the y-direction zoomed to a section of the stack. (B) Schematic of stack box arrangement in test-rig and different heat transfer phenomena between the stack box and the furnace.

gas was neglected. A sophisticated passive area model was developed by researchers within the group[23] and will be included in future work.

Figure 1 also shows how heat transport within the reactor occurs in the x (flow), y (perpendicular) and z (vertical) directions through the thermal interfaces. Thermal connections equalise temperature and balance the total heat flow. Coupling all layers in an RU to a single interface at each side, ensured the same temperature at the boundary and reduces the number of interfaces interacting directly with the surroundings. Along the *x*-axis, each RU is thermally connected to the passive area via conductive heat transfer at the inlet and outlet point. In the z-direction each RU is thermally connected through their boundary ICs to another, also through conduction allowing the model to also predict the vertical temperature profile. In the y-direction, the ICs and PEN are connected to a single external interface for every RU. At the very top and bottom of the reactor and y-direction sides, interfaces are used to interact with the surroundings of the reactor through heat transfer models to define the system boundary conditions. Heat transfer in the y- and z-direction are discretised in the x-direction.

Furnace model.—Boundary conditions for the reactor are provided through heat transfer with its fixed temperature surroundings. Heat transfer from the reactor to the environment is known as heat loss and expected to have a negative impact on the performance. The experimental analysis of the 10 cell SOC reactor was performed in a typical furnace environment which was used for the validation of the model. For the experiments, the SOC reactor as described above was placed inside a metal box (referred to as stack box from here on) with gas inlet piping and outlet piping for both fuel and air.

The stack box was mounted inside a pressurised furnace of the pressurised SOC reactor testing facility. To ensure gas tightness, and

avoid leakages, a steel block weighing 120 kg was placed on top of the stack box. A detailed description of the test rig and arrangement of the stack box within the test rig is provided in Riedel et al.[29] The schematic of the stack box as mounted in the test rig and the different heat transfer phenomena between the stack box and surrounding furnace environment is shown in Fig. 2B. As the stack box was not insulated inside the furnace, heat transfer to the surrounding environment up to the furnace wall, which was assumed to have a fixed temperature, was possible. Conductive heat transfer occurs along the z-direction between the top of the stack box to the steel block and bottom of stack box to the support. Radiative heat transfer occurs between the furnace wall, stack box, support and steel block in all directions. The radiative heat transfer was evaluated using Eq. 14.

$$\dot{Q} = \epsilon_i \cdot \sigma \cdot (T_{furnace}^4 - T_i^4) \cdot A_i, \qquad [14]$$

Convection in the y-direction was neglected due to the small heat transfer area in the channels and larger heat transfer potential in the IC and PEN. On each side, y-direction heat transfer was lumped to interact with an external model to represent the total heat transfer from that side. This therefore reduces the accuracy in terms of temperature profile at this boundary, however, due to the small area, this was not deemed significant. To complete the boundary conditions, a lumped thermal resistance was calculated for the different heat transport mechanisms as shown in the Fig. 2A for the heat transfer between the stack and furnace. Thermal resistance of heat conduction was calculated with Fourier's law, and of radiation can be estimated with Eq. 15, which is the first order Taylor series expansion of the radiation term. Material properties were taken from several literature sources. However, as some parameters incorporate multiple materials, it was difficult to represent them based on literature data. Hence, a nonlinear least squares fitting was performed to find suitable constant parameters based on the SOFC experimental measurements, and fixed to represent the test-rig environment for other cases.

$$R_{th} = \frac{1}{4\epsilon_{box} \cdot \sigma \cdot T_{furnace}^3 \cdot A} \qquad [15]$$

Simulation Methodology

The study was performed in three forms utilising the reactor and test-rig model outlined above. First, the model was validated against the steady-state and dynamic experimental measurements performed by Riedel et al.[3,29] on a 10-cell electrolyte supported cell (ESC) reactor (Sunfire GmbH, Dresden, Germany) in a pressured environment. From the validated results, further analysis of the reactor was performed, especially focussing on the behaviour of the reactor under coEl and the thermal phenomena within the reactor and surroundings. Finally, the model was used to predict reactor performance at elevated pressures above those used in the experiments.

Steady-state model validation.—The model validation was performed for three operating conditions of SOFC, steam-, and coEl for several current densities with operating parameters taken from the experimental studies. For SOFC, a reactant conversion (RC) of 55% and air utilisation (AU) of 15% was used. For the electrolysis runs, a fixed air flow of 10 slpm was used. Furthermore, for coEl two feed molar compositions of 60:30:10 (603010) and 45:45:10 (454510) of H_2O: CO_2: H_2 were used as well as two pressures of 1.4 bar and 8 bar, as was done in the experimental study. For each run, the respective RC was kept constant, by varying the current density and mass flow rate according to Faraday's Law. Each cell was discretised into 10 control volumes along the flow direction, resulting in a 1D+1D mesh of 520 control volumes including the different layers of the cell and the end plates just for the reactor. To

achieve steady-state, the model was allowed to run for 1e6s for each current density to ensure an average temporal derivative of near zero ($\sim$1e–10 s^{-1}), this took approximately 48 s per steady-state point on a laptop with a 2.7 GHz quad core Intel i7–6820HQ CPU and 32GB RAM, demonstrating the high accessibility for the reasonable detail of the model provided by the simulation framework.

For the model validation, the voltage at the centre cell (cell 5) and temperature at the central point (cell 5, mid-point) were used as the main characteristic values. Additionally, the outlet dry gas composition was also measured in the experiment and was used for the validation. Furthermore, the impact of implementing the coEl model was also analysed through the lens of the characteristic points.

Results and Discussion

This section outlines the various results obtained from the simulation studies. Starting with the results of the model validation based on the characteristic U(i) and T(i) curves for different operating conditions, followed by the analysis of the phenomena occurring in the reactor obtained from the model results, and closing with a discussion on results obtained for pressurised coEl outside the validated range.

Model validation.—The steady state U(i) and T(i) curves are important to characterise the reactor performance, while the composition-current curves are important to demonstrate the ability of reaction kinetics and mass flow relations to represent the reactive multi-species transport phenomena within the reactor. Hence, the reactor model was validated against experimental results in SOFC and SOEC operation mode. The developed coEl model was also compared against an SOEC model neglecting electrochemical CO_2 electrolysis with the same feeds to evaluate its impact at larger scales. Validation for dynamic operation for CO_2 electrolysis is also illustrated here.

Steady state operation.—Figure 3 illustrates that the model developed in this work can generally simulate steady state processes for both SOFC and SOEC mode with high accuracy. The average deviation of voltage at the centre cell was ca. 23.3 mV (2.87%) for steady state SOFC points, and ca. 16.8 mV (1.38%) for steady state H_2O/H_2 SOEC points. This small deviation of cell voltage can be attributed to the deviation of the cell temperatures; where the maximum deviation found for the SOFC simulations was ca. 2.6 °C (0.24%) and ca. 5.54 °C. (0.50%) for the steam electrolysis simulations, observed under the highest current densities. The model is clearly able to demonstrate the difference in performance between steam SOEC and coEl as shown in the experimental measurements. The average deviation of the centre cell voltage was ca. 8.9 mV (0.69%) with a maximum deviation of 24 mV (1.76%) and average temperature deviation of ca. 5.5 °C (0.51%), with a maximum deviation of 7.8 °C (0.73%). The largest deviation in cell voltage was observed at highly exothermic conditions, corresponding with the temperature deviation observed.

Figure 3 also illustrates that the model can predict coEl reactor outlet gas compositions to reasonable accuracy. The average deviation of the outlet dry gas compositions was less than 1 mol% for all components. Furthermore, the experiment and simulation results indicated that the gases reach equilibrium at the reactor outlet, where the outlet gas temperature was used to calculate equilibrium. Errors against experimental results were largest at the lower current density range which may be attributed to measurement errors. In order to maintain a constant RC of 0.7, the flow rates of the feed gases had to be manipulated with the current density. At low current densities, it was difficult to control the low feed flowrates through the mass flow controllers, leading to inconsistent measurements for the gas compositions here. Nevertheless, these errors are negligible for the applicability of the model.

These small deviations are likely due to the simplifications of the internal and external heat transfer, where fixed values for heat transfer coefficients were used. Additionally, ignoring preheating of gases and simplifying resistances in the passive area and sides also limit the flexibility of the model to be fitted to minimise errors. The influence. of external heat transfer on the axial temperature profile is detailed further below, while the vertical temperature profile and the influence of including the passive area model is briefly analysed in the supplementary information. It should also be noted that the thermocouples in the experiment were manually inserted into the outlet side of the AC, which allows for the possibility of hot/cold spots affecting the measurement results. Nevertheless, the relatively low errors in the model results illustrate the high accuracy of the model despite the simplifications, allowing for its use in understanding the internal processes and predicting behaviour in different operating conditions.

Comparison of co-electrolysis model with steam electrolysis + RWGS.—Figure 4 depicts the comparison of the experimental T(i) and U(i) results and the curves simulated with the full co-electrolysis model and a reduced model that only includes electrochemical steam electrolysis and the RWGS reaction. The OCV error was smaller in the coEl model, staying within a 0.1% error margin whereas the steam electrolysis model had OCV errors up to 0.5%, suggesting that the implementation of the coEl model can further improve the OCV calculation accuracy. However, Fig. 4 illustrates that the T(i) and U(i) results for both models are nearly identical, with the same causes for deviations outlined above. These results demonstrate that the application of a reduced steam electrolysis + RWGS model is sufficient to describe the electrochemical and thermal behaviour of the stack with high accuracy. In addition, this approach has the benefit of solving faster as it contains fewer equations which is particularly useful for running large system simulations.

Dynamic electrolysis.—In this case, rather than simulating until a steady state was found to match the steady state U(i) curves, the applied current density was increased at a fast rate of 2.57 mA·cm^{-2}/s for three conditions: (1) with a fixed feed composition of 90% CO_2 and 10% CO to correspond with the experiments conducted in;[42] (2) 45% CO_2, 45 H_2O, and 10% H_2 at 1.4 bar corresponding to experiments in;[3] and (3) 45% CO_2, 45% H_2O, and 10% H_2 at 8 bar corresponding to experiments in.[3] Figure 5 shows that the model was able to follow the trends of increasing voltage and variations in cell temperature observed in the experimental measurements very closely but deviations grew during the ramp for the three cases presented. For the CO_2. case an overall an average error of 1.15 K (0.15%) and 17.03 mV (1.6%) was observed with maximum deviations of 3.17 K (0.41%) and 60.97 mV (4.19. %) against a 9th order polynomial fit of the experimental data. This polynomial fit was necessary match the results of the variable step ODE solver simulation results to the experimental measurement points. For the coEl cases, against a 9th degree polynomial fit, integral average error of 4.27 mV (0.44%) and 0.44 K (0.06%) was observed for the 1 bar case and 5.34 mV (0.47%and 1.7 K (0.21%) for the 8 bar case; with maximum deviations of 11.92 mV and 2.06 K for the 1 bar case and 5.34 mV and 3.05 K for the 8 bar case.

While these deviations are small, they can be further minimised with more accurate kinetic and thermal parameters. The sensitivity analysis (see supplementary information) shows that the reaction order and activation energy have strong influence on the fit against experimental data. Further studies will investigate the use of experimental measurements in developing better kinetic parameters for the model.

SOC reactor performance analysis.—The characteristic curves utilised in the model validation, provide a high-level view of the reactor performance based on measurable variables. However, the model can provide a deeper understanding of the phenomena occurring within the reactor which may be difficult to measure, especially for larger reactors. This section will detail the key phenomena that occur within the reactor from the simulation runs presented above. First, the thermal behaviour
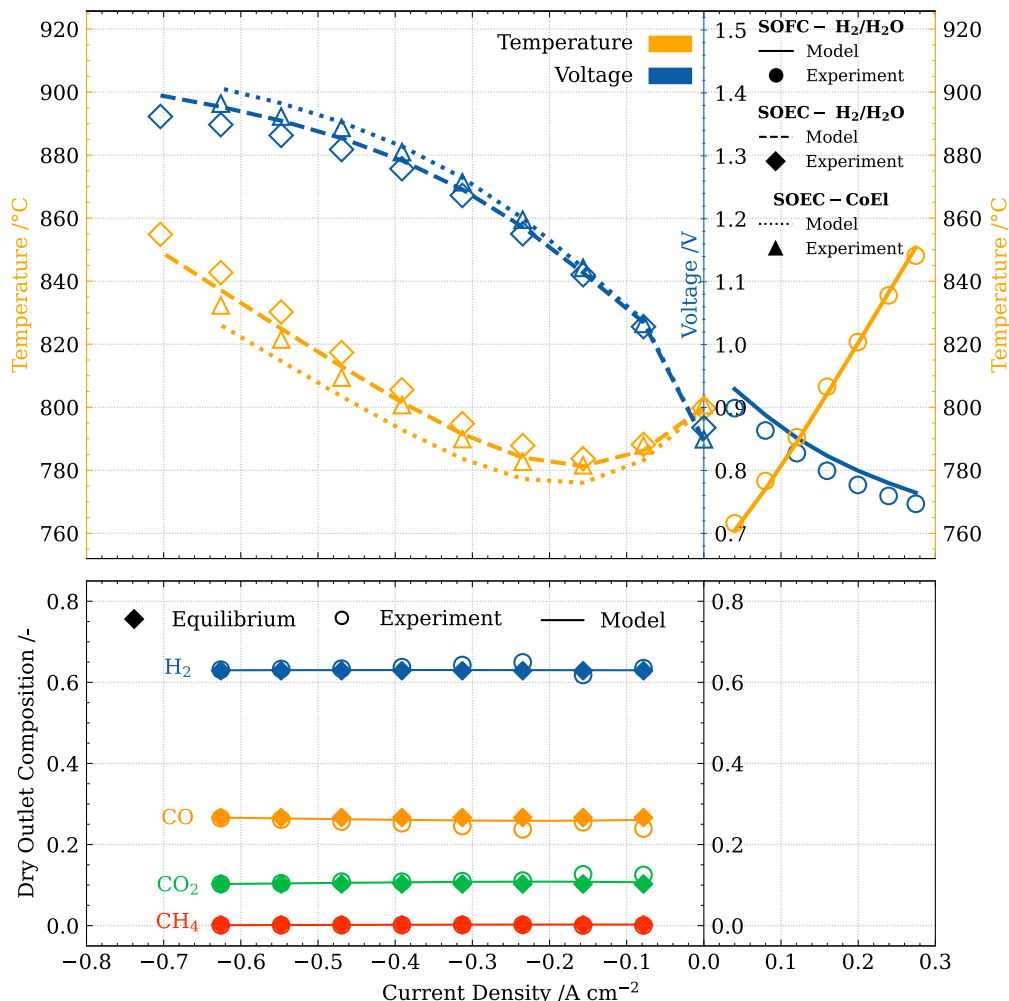
Figure 3. (Top): Steady-state U(i) and T(i) curves from model against experimental results for SOFC (p = 1.4bar, T_f = 750 °C, inlet x_{H_2}: x_{N_2} = 40: 60, RC = 0.55), steam electrolysis (p = 1.4bar, T_f = 800 °C, inlet x_{H_2}: x_{H_2O} = 10: 90, RC = 0.6) and co-electrolysis (p = 1.4bar, T_f = 800 °C., inlet x_{H_2O}: x_{CO_2}: x_{H_2} = 60: 30: 10, RC = 0.7). (Bottom): Steady-state dry outlet composition during co-electrolysis at the same conditions as plot above, comparing model, measurements and equilibrium.
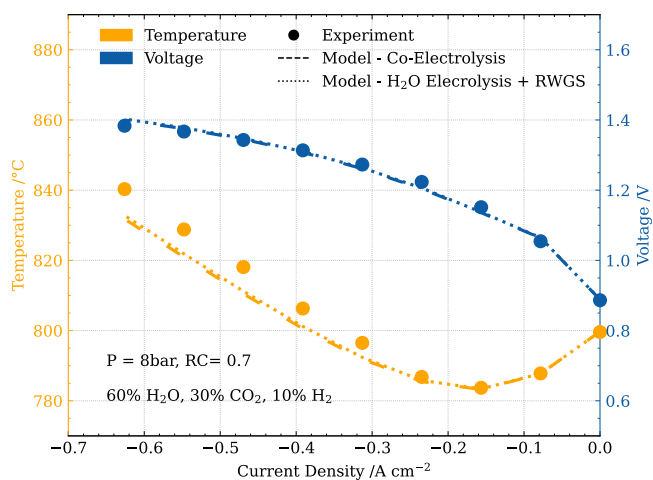

Figure 4. Steady-state U(i) and T(i) curves of SOC reactor under co-electrolysis comparing the model including CO_2 electrolysis (Co-Electrolysis) with the model neglecting CO_2. electrolysis (H_2O Electrolysis + RWGS) and experimental measurements.

and coupled interactions between the heat transfer and electrochemical behaviour are presented, and then the coEl behaviour is analysed with a focus on the CO_2 reduction pathway and how it may vary with operating conditions.

Thermal behaviour.—Temperature has a significant influence on multiple processes in the reactor and can be influenced through various operating conditions, e.g. current densities, as presented above. Figure 6 illustrates the range of temperatures that can occur in the reactor, dependent on various flow phenomena within the different layers of the RUs. For the endothermic operation, with low current density, a cold point resides in the middle of cell 5 due to heat transfer from the furnace through the other faces compensating the endothermic electrolysis reaction as well as the relatively lower flow rate. While for exothermic operation, the hot point resides near the outlet, due to higher flow rates keeping the inlet zone cooler. This is also observed for the single cell distribution shown in the middle row. Despite thermoneutral operation exhibiting a uniform temperature distribution throughout the reactor, a small internal thermal gradient exists within the layers of the cells, due to the low residence time of the air flow and may be countered with air flow management. The general temperature profile in cell 5 is nonlinear and may be approximated as parabolic in x- and z-
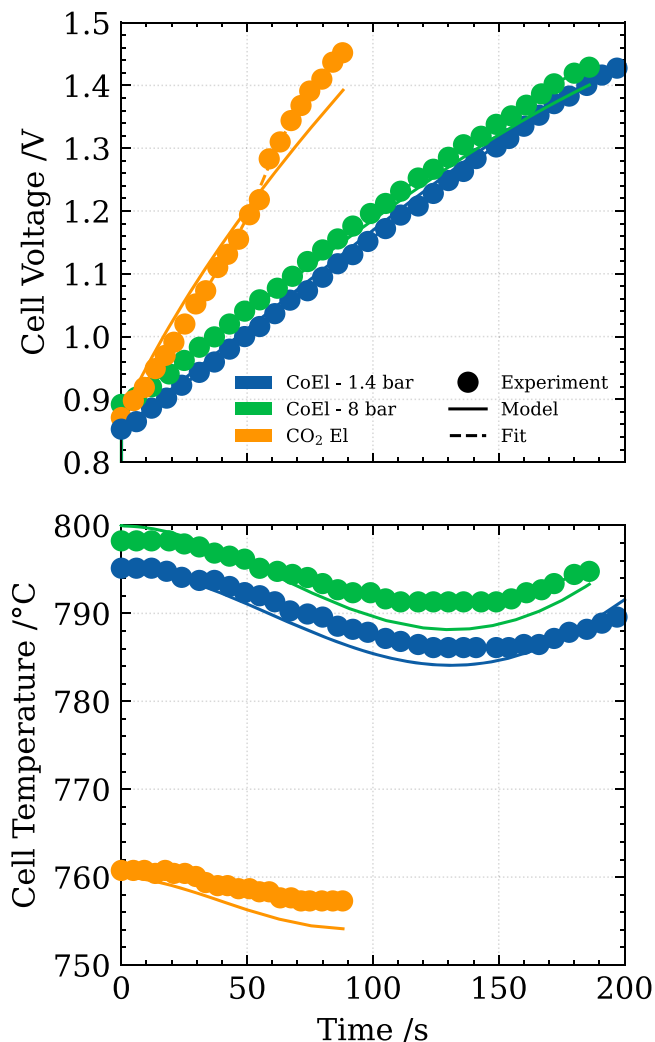
Figure 5. Dynamic operation characteristic UI (top) and TI (bottom) curves at cell 5 under three operating conditions of (1) CO_2. electrolysis (90% CO_2., 10% CO, T = 760 °C, p = 1.4 bar, RC = 0.5); (2) coEl (45% CO_2., 45% H_2O, 10% H2, T = 800 °C, p = 1.4 bar, RC = 0.75); 3) coEl (45% CO_2., 45% H_2O, 10% H2, T = 800 °C, p = 8 bar, RC = 0.75) all with a constant ramping current density of $\Delta i/\Delta t$ =2.6 mA·cm^{-2}/s compared with experimental measurements from[29] and[3].

direction due to the highly conductive heat flow from the solid materials and sources/sinks of electrical flow and electrolysis.

The total cell area specific resistance (ASR) distribution over the height of the stack follows the temperature profile with increasing values towards the middle of the stack in endothermic operation, similar values in isothermal operation, and increasing ASR values towards the top and bottom in exothermic mode. Moreover, Fig. 6 shows that the total ASR for all RUs is at all operating points dominated by the ohmic resistance which is a common behaviour for the modelled electrolyte supported cell type with 90 μm thick 3YSZ electrolyte.[36,43] At the operating temperatures >800 °C that are required to achieve sufficiently high ionic conductivity, the electrode kinetics are relatively fast and display smaller resistance contributions that amount to ~20% of the ASR of the RUs. With regards to the relative electrode contributions, the Ni/CGO fuel electrode resistance is significantly higher than the air electrode resistance which is consistent with experimental results on cell level.[36]

Although higher current densities and the resulting higher temperatures reduce the cell losses, operating above the thermoneutral point reduces the efficiency, as the additional power input is converted to heat which cannot be utilised for the heat demand of the

endothermic co-electrolysis reaction. Therefore, it is imperative that the temperature in the reactor is controlled to not only minimise thermal gradients but also maximise efficiency. This is best achieved through the knowledge of the internal energy balance of the reactor, which can be manipulated in several ways (e.g. varied air flow or temperature) and occurs through all faces, but at different rates.

Figure 7 illustrates the results of a reduction study, where heat transfer through the different planes of the reactor was eliminated step-wise starting from y-plane, to z- plane then completely adiabatic under fuel cell operation. As expected, for an adiabatic process, the cell temperature rises greatly due to the generated heat from the exothermic reaction remaining in the cell and limited by the convective heat transfer to the fluids. Enabling heat transfer through the z-direction significantly affects the value of the maximum temperature and marginally flattens the temperature distribution. Additional heat transfer between the reactor and surroundings along x-direction then drastically influences not only the value of maximum temperature but also the position of the hot spot. The reactor outlet temperature is typically used as a measured variable to control and regulate the reactor temperature. Under high heat loss scenarios, the hot-spot during exothermic operation shifts towards the centre of the cell which can lead to having temperatures higher than the allowable limit of the materials used (e.g. glass sealings), potentially damaging the SOC. The impact of additional heat transfer along the y-direction is relatively weak, because the reactor used in this work consists of only 10 cells resulting in a small surface area in the y-plane. Neglecting this heat transfer axis may be beneficial for faster simulation time for small reactors. Overall, the presented results display the great influence of heat transfer between the reactor and its surroundings via the various faces, through its influence on the temperature distribution of the centre cell.

Figure 7 also shows that although the centre point temperature is close to experimental measurements, the predictions away from the centre point deviate while following the profile suggested by the measurements. This may be due to the simplified heat transfer model for the passive area whose influence can also be seen in Fig. 6, where a uniform vertical temperature profile at the reactor inlet and outlet can be seen. With better heat transfer models between the stack and environment, a closer temperature profile may be observed. This would improve voltage predictions, as it is evident that the overpotentials are largely temperature dependent.

Reactor performance in co-electrolysis operation.—Particularly important is the composition leaving the reactor as it will affect processes downstream. Figure 8 shows that the model predicted gas compositions within the cell, follow the same trend as that observed from an equilibrium model. This overlap is a result of the fast kinetics at the operating conditions and limited by the temperature driven equilibrium constant. The fast production rate of CO at the entrance imply that the reactor conditions greatly favour the RWGS reaction which can also be observed in Fig. 9. This interaction between the electrochemical and thermochemical reactions is also observed in the total conversion of CO_2. The electrochemical conversion, based on Faraday's law relating the molar input and current density was 0.7 however, the total conversion of CO_2 deviates from this slightly ranging between 0.67–0.73. This deviation is a result of the thermochemical equilibrium and is therefore influenced by the temperature and pressure. At lower temperatures, the tendency for RWGS is lowered but still surpasses the 0.7 conversion. At higher pressures, H_2 is converted to CH_4 and therefore its availability for RWGS is reduced thereby reducing the conversion—this is countered in exothermic operation as the methanation reaction is not favoured at higher temperatures.

When looking into the pathway for CO_2 consumption, Fig. 9 (top) shows that RWGS dominates throughout the length of the cell for all conditions which aligns with most literature on the matter as explained above. However, this extent is largest at the inlet (over 80%) and dramatically plateaus to ~60%–70% for the remainder of
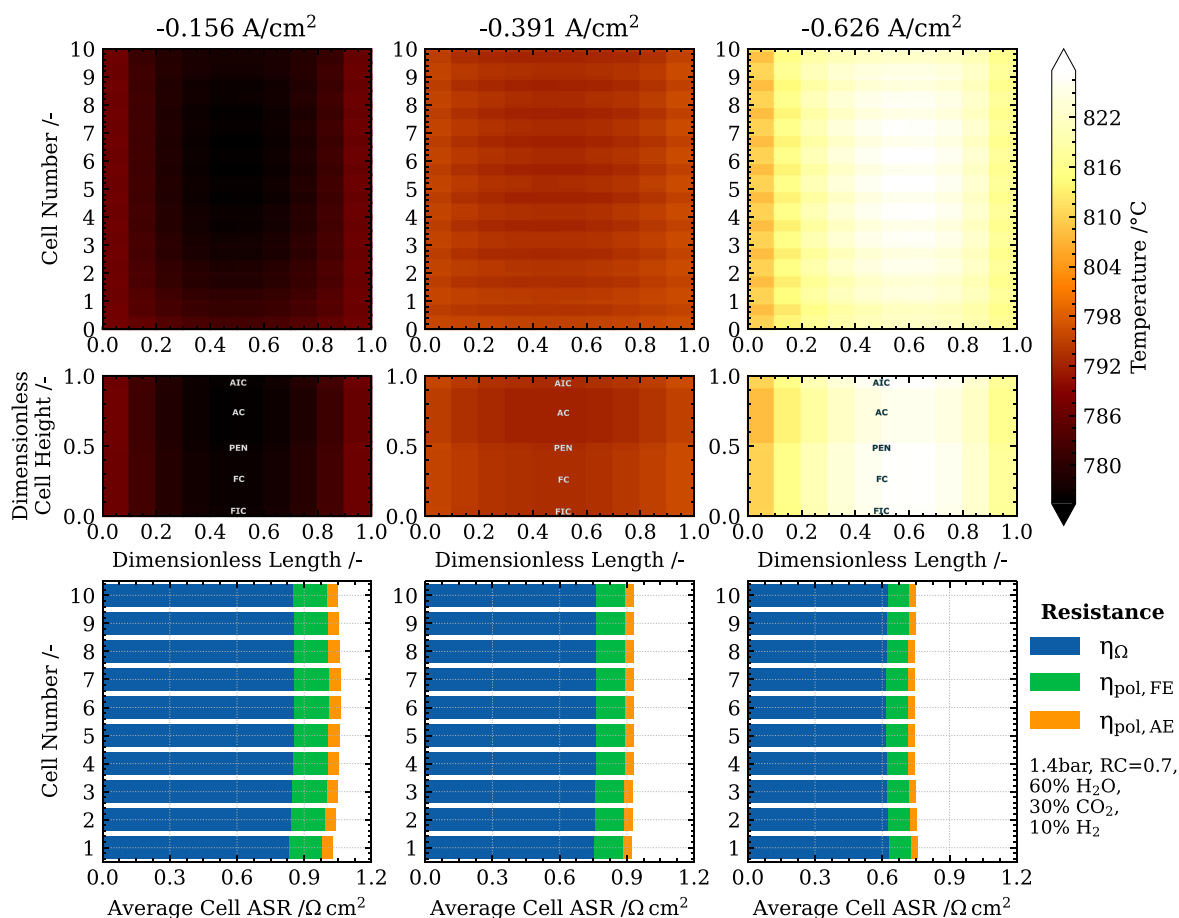
Figure 6. Thermo-electrochemical analysis of reactor (Top): Distribution of temperature in 10-cell reactor under endothermic, thermoneutral and exothermic conditions. (Middle): Distribution of temperature in cell 5. (Bottom): Average cell area specific resistance (ASR) divided by share of each loss mechanism.
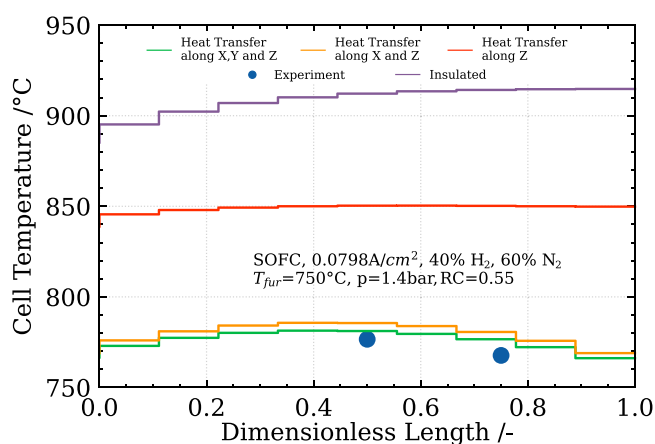

Figure 7. Effect of heat transfer between reactor and surroundings at cell 5 temperature distribution (**SOFC**; $p = 1.4bar$., $T_{furnace} = 750$ °C., inlet $x_{H_2}: x_{N_2} = 40: 60$., $FU = 0.55$, $j = 0.0798A$/cm².).

the cell length which can be observed from a large step—which arises from the high CO_2 content in the feed reacting with the H_2 in the feed due to the large driving force for RWGS. Although RWGS dominates, these results show that electrochemical CO_2 reduction may occur to. a significant extent during co-electrolysis, ranging from 24%–34% of the total CO_2 conversion (Fig. 9, middle) which coincides with the findings of.[3] Near thermoneutral operating conditions were used for the conditions shown in Fig. 9 to minimise influence of temperature. Having higher CO_2 content lowers the

extent of CO_2 consumption via CO_2 electrolysis by ∼8% likely due to a higher driving force for the RWGS reaction. Overall pressure increases the extent of Co_2 electrolysis by only ∼1%. However, locally a larger influence of pressure can be observed with a pronounced increase of electrochemical CO_2 electrolysis towards the end of the channel at higher pressure. This increase with pressure follows in line with the production of CH_4 illustted in Fig. 8 suggesting that it is a result of the reduction in rate of RWGS due to hydrogen being consumed in the methanation reaction. These effects extend throughout the stack, and as illustrated in Fig. 6 large variations in temperature may occur and therefore impact the equilibrium. concentrations at the outlet and affect the syngas ratios. Nevertheless, inlet feed composition is the dominant factor in determining the outlet syngas ratio as well as the electrochemical phenomena.

The shares of the two electrolysis reactions illustrated in Fig. 9 (bottom) show that steam electrolysis occurs to a significantly larger extent than CO_2 electrolysis. This dominance varies with inlet feed composition with a higher CO_2 content. resulting in a near 1.5% reduction of the share of electrochemical CO_2 reduction likely due to the lower steam content. This is a result of the complex interplay between H_2O electrolysis, CO_2 electrolysis and RWGS reaction where the two latter reactions are both promoted by an increase in CO_2 partial pressure. In addition, a small near linear decrease in the current density ratio is also observed over the cell length, likely due to the reduction in steam content over the cell length and the effect of temperature on the equilibrium of RWGS towards the end of the cell. A small influence of pressure is also observed, whereby the share of steam electrolysis is lowered marginally at 8 bar. This is likely due to a marginal improvement in CO_2 electrolysis kinetics as observed from the top two plots in Fig. 9.
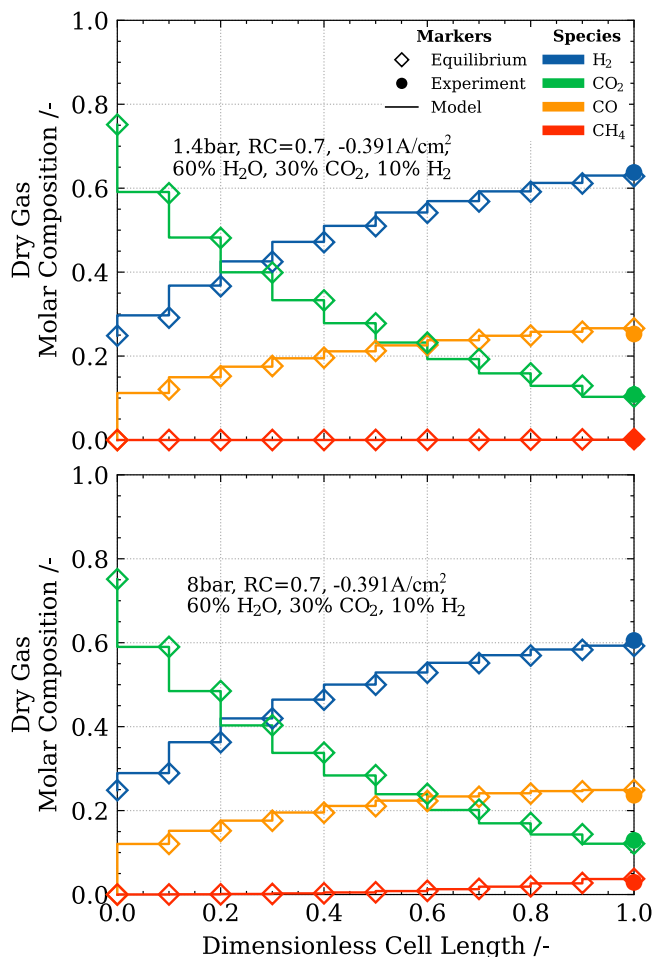
Figure 8. Variation of dry gas composition along length of cell 5 according to model, compared to equilibrium and measured outlet composition fo. all steady state co-electrolysis experiment runs at 1.4 bar (top) and 8 bar (bottom).
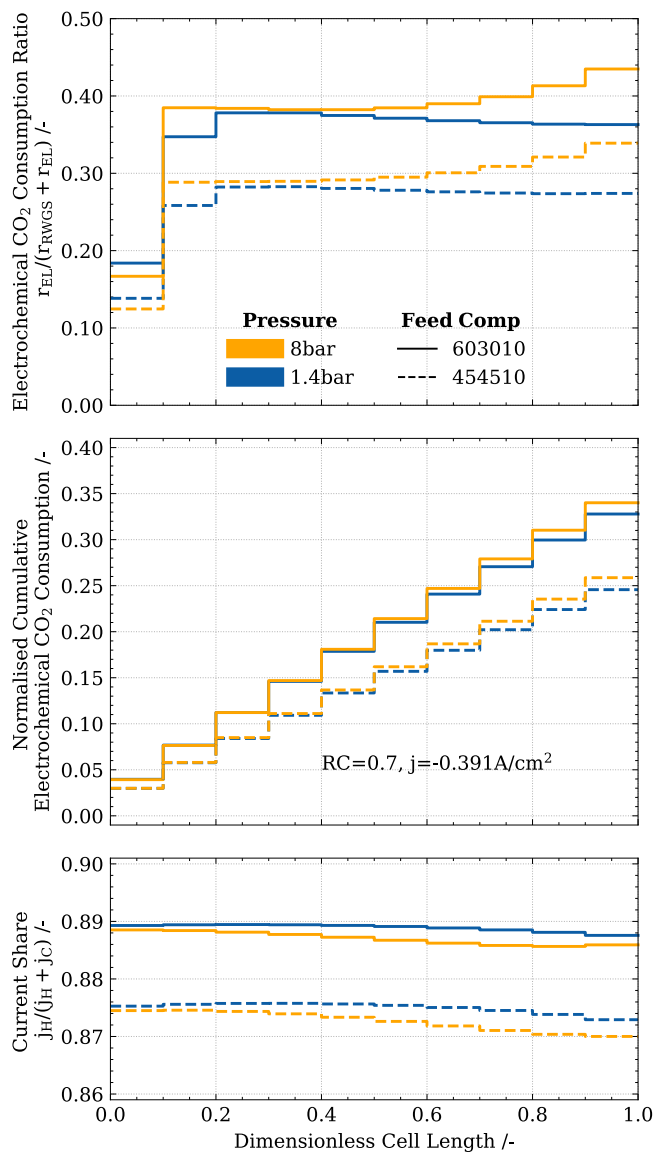

Figure 9. Electrochemical kinetics variation over length of cell 5 (Top): Local variation of electrochemical CO_2 consumption over total consumption under co-electrolysis operation at thermoneutral conditions. (Middle): Cumulative consumption of CO_2 via electrolysis over cell length. (Bottom): Share of current density for steam electrolysis at FE.

As shown in Table II, the parameters a and b in Eq. 11 for the CO/CO_2 reaction were assumed to be equal to the ones for the H_2/H_2O reaction since no detailed experimental stack data for the independent variation of CO and CO_2 was available. These empirical parameters are generally a function of the rate-determining steps in the underlying reaction mechanisms. Grosselindemann[35] on the other hand, used the same form in Eq. 11 for the same cell design as used in the in-house experiments, and found linear dependencies with temperature in their reaction indices for most electrochemical reactions occurring in the. FE and AE. However, due to the discrepancy with internal fitting results, these values were not taken for this work but briefly analysed in the supplementary information showing large differences to the experimental measurements presented here. The elementary reaction mechanisms have been widely investigated for Ni/CGO fuel electrodes, however, there is no clear consensus in literature. Some studies suggest that for the H_2/H_2O reaction on Ni/ceria electrodes, the Ni phase acts solely as a current collector and the electrochemical reaction takes entirely place on the ceria surface, that is, the double phase boundary (DPB) to the gas phase.[44] However, in other studies Ni was also observed to contribute to the electro-catalytic activity of a Ni/CGO electrode suggesting an extension of the electrochemical reaction zone to the triple phase boundary between Ni|CGO|gas phase.[45] Most likely, the relative contribution of the DPB and TPB pathways during the H_2/H_2O reaction varies strongly on the composition and microstructure of the electrode. For optimized state-of-the-art Ni/CGO

fuel electrode the electro-catalytic role of Ni indeed seems to be small. The CO/CO_2 reaction can also occur on the doped ceria surface,[45,46] however, the role of Ni on the electro-catalytic activity during the CO/CO_2 reaction was reported to be more pronounced suggesting the reaction to predominantly take place at the TPB.[47,48] This discussion demonstrates that there are potentially large differences in the nature of the rate-determining steps indicating also a difference in the parameters a and b for the different reactions. The parameters will be adjusted through future work carried out by co-members of the authors' research group directed at CO_2 electrolysis.[42]

A sensitivity analysis investigating how the influence of the kinetic parameters affect the results presented here is provided in the supplementary information, and shows that the reaction order and activation energy can have significant influence on the rate of electrochemical reaction. Thus, the values in Fig. 9 could change once refined kinetic parameters become available. Nevertheless, the discussed dependencies of CO_2 consumption pathway on pressure,

inlet gas phase composition and channel position should still remain valid and provide a qualitative understanding of the coEL reactor behaviour.

Elevated pressure co-electrolysis.—In addition, the validated coEl model can be used to predict reactor behaviour at other possible operating points, in this instance higher reactor pressures for the direct production of high-pressure syngas. These simulations were used to study the reactor behaviour under operating conditions that may be employed for wider uses of high temperature SOC reactors. The simulations were performed for the same current densities as the steady state validation above, at a constant RC of 0.7 for various operating pressures with a coEl feed, and the furnace and feed temperatures set to 800 °C. Figure 10 demonstrates that increasing stack pressure results in significant changes to the characteristic behaviour. First, the positive logarithmic dependence of the thermodynamic electricity demand, ΔG, on pressure results in a higher open circuit voltage (OCV).

Furthermore, as mentioned above, higher pressures shift the equilibrium towards the exothermic methanation reaction. This increases the temperature within the cell greatly, resulting in lower overpotentials and cell voltage. This reduction is especially significant at current densities greater than $0.16 \, A \cdot cm^{-2}$ where the cell voltage relation with pressure is inverted when compared to the OCV. The additional heat generation from the exothermic reaction leads to exponential decay of thermoneutral voltages expressed in the fitted expression of $V_{TN}(p) = 0.265 \exp(-0.028p) + 1.089$ V. More specifically at 50 bar and 100 bar voltage values of 1.157 V and 1.105 V, respectively were predicted, which are significantly lower than the thermoneutral voltage value of $\sim$1.35 V commonly observed at ambient operation. This, also means lower current densities of $0.17 \, A \, cm^{-2}$ at 50 bar and $0.1 \, A \, cm^{-2}$ at 100 bar are required to achieve thermoneutral behaviour, here demonstrated through the characteristic centre-point temperature matching the furnace temperature. This would in turn result in lower syngas productivities when operated at the generally preferred thermoneutral operating point. Productivity can be increased with larger reactors, leading to higher costs; or with higher current densities, resulting in an exothermic process. Although the additional heat may be useful for certain processes, this reduces the reactor efficiency as well as the long-term stability of the cells, due to added thermomechanical stresses.

Furthermore, with higher rates of methanation, the effort in producing syngas becomes inhibited as illustrated by the lower hydrogen content with higher pressures in Fig. 10. For certain processes such as methane synthesis, this may be advantageous, since a smaller downstream reactor can satisfy the conversion demand. However, for most other processes that require syngas, such as Fischer-Tropsch synthesis, the consumption of syngas to produce methane restricts to system-wide productivity, thereby possibly reducing system efficiency. Thus, the present calculations demonstrate that pressurized co-electrolysis may face techno-economic limitations at higher operating pressures.

It should be noted that the model has only been validated for stack pressures of 1.4 bar to 8 bar therefore the predictions beyond 8 bar are limited by the assumptions used e.g. ideal gas, negligible pressure drops, laminar flow, diffusion models, reaction kinetics and no coking. At higher pressures, some of these assumptions such as ideal gas, may not hold for all of the species considered and the consideration of coke formation may become more relevant. To be confident of the results observed in Fig. 10, experimental validation would be desired and is recommended for future work. Nevertheless, these results are useful for the design of coEl SOC reactors for elevated pressures, as costs increase significantly for every marginal increase in design pressure due to materials and operating difficulty, hence enabling cost minimisation and performance optimisation.
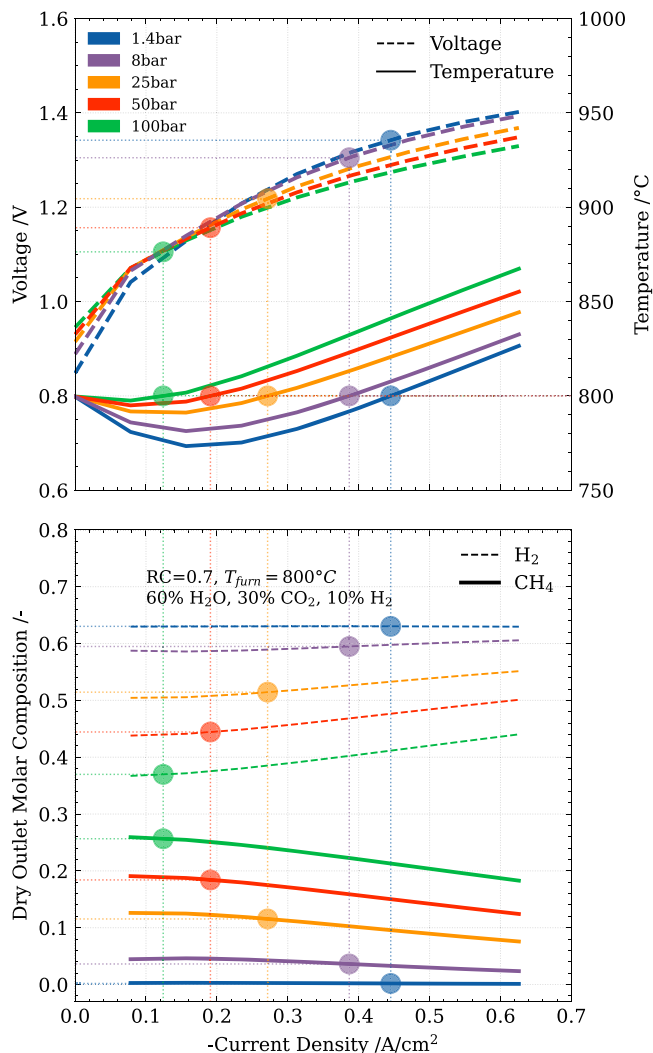

Figure 10. Model predicted TI and UI curves for cell 5 (top) and outlet dry hydrogen and methane molar compositions (bottom) for co-electrolysis operation with different operating pressures indicating the change in thermoneutral voltage at furnace temperature of 800 °C.

Conclusions

To better understand CO_2 and coEl operation for its wider adoption, a 1D+1D SOC reactor model was further developed to predict steam, CO_2 and coEl behaviour. Validation over steady-state for SOFC and SOEC including coEl, and dynamic CO_2 electrolysis operation showed high levels of accuracy with experimental results with respect to cell voltages, temperatures and compositions. Deviations were largely assumed to be due to external heat transfer simplifications and kinetic parameters for CO_2 electrolysis. The validated simulation results were used to investigate various phenomena during coEl. Chiefly, for the literature-based parameters for CO_2 electrolysis kinetics, it was found that CO_2 consumption via RWGS was the dominant CO_2 reduction path, but CO_2 electrolysis occurs to significant rates (up to 35% of total CO_2 conversion). Experimentally derived kinetic parameters are needed to confidently conclude this relationship for the Ni-CGO FE material modelled here.

To demonstrate the wide usability of the reactor model, simulation for process system relevant operating conditions, namely high-pressure coEl was performed. The elevated pressure operation promoted exothermic methanation resulting in various

thermochemical effects, especially on the cell voltage and thermo-neutral-isothermal current density. Suggesting that, pressurised operation may be beneficial, however not at the higher ranges due to negative effects on productivity during thermoneutral operation, which limit syngas production. Research in finding this optimal point through this model for large systems is being carried out by the authors.

Solid oxide cell reactors come in various forms and the modelling framework developed here allows for extension to analyse behaviour in different cell, stack and module designs and operating conditions. The modelling of SOC reactors for these designs and operating conditions advance deeper understanding of their benefits and limitations from a thermohydraulic standpoint and widen the adoption of this technology. In this respect, the model presented here may be used to develop operation strategies for various SOC reactor systems in different operating regimes such as; renewables coupling, electrolysis with hydrocarbon containing feeds, and fuel cell system operation, among others. This work is ongoing by co-members of the author's research group.

ORCID

F. Sedeqi https://orcid.org/0000-0003-2883-6494
M. Riegraf https://orcid.org/0000-0002-0383-2545

References

1. IEA, Renewable Energy Market Update: Outlook for 2023 and 2024, International Energy Agency, 2023. [Online]. Available https://iea.org/reports/renewable-energy-market-update-june-2023 (12.07.2024).
2. G. Min, S. Choi, and J. Hong, "A review of solid oxide steam-electrolysis cell systems: thermodynamics and thermal integration." *Appl. Energy*, **328**, 120145 (2022).
3. M. Riedel, M. P. Heddrich, and K. A. Friedrich, "Experimental analysis of the co-electrolysis operation under pressurized conditions with a 10 layer SOC stack." *J. Electrochem. Soc.*, **167**, 024504 (2020).
4. M. C. Williams, S. D. Vora, and G. Jesionowski, "Worldwide status of solid oxide fuel cell technology." *ECS Trans.*, **96**, 1 (2020).
5. L. Dittrich, M. Nohl, E. E. Jaekel, S. Foit, L. G.-J. de Haart, and R.-A. Eichel, "High-temperature co-electrolysis: a versatile method to sustainably produce tailored syngas compositions." *J. Electrochem. Soc.*, **166**, F971 (2019).
6. K. Schwarze, T. Geißler, M. Nimtz, and R. Blumentritt, "Demonstration and scale-up of high-temperature electrolysis systems." *Fuel Cells*, **23**, 492 (2023).
7. N. S. Kalib, A. Muchtar, M. R. Somalu, A. K.-A. Mohd Ihsan, N. A. Mohd Nazrul Aman, and J. C. Wen Mah, "Influence of heat transfer on thermal stress development in solid oxide fuel cells: a review." *Journal of Advanced Research in Fluid Mechanics and Thermal Sciences*, **54**, 175 (2020), [Online]. Available https://akademiabaru.com/submit/index.php/arfmts/article/view/2447.
8. C. M. Stoots, J. E. OBrien, S. J. Herring, and J. J. Hartvigsen, "Syngas production via high-temperature coelectrolysis of steam and carbon dioxide." *J. Fuel Cell Sci. Technol.*, **6**, 011014 (2009).
9. M. Riedel, M. P. Heddrich, and K. A. Friedrich, "Analysis of pressurized operation of 10 layer solid oxide electrolysis stacks." *Int. J. Hydrogen Energy*, **44**, 4570 (2019).
10. L. Magistri, R. Bozzo, P. Costamagna, and A. F. Massardo, "Simplified versus detailed solid oxide fuel cell reactor models and influence on the simulation of the design point performance of hybrid systems." *J. Eng. Gas Turbines Power*, **126**, 516 (2004).
11. A. Banerjee, Y. Wang, J. Diercks, and O. Deutschmann, "Hierarchical modeling of solid oxide cells and stacks producing syngas via H_2O/CO_2 Co-electrolysis for industrial applications." *Appl. Energy*, **230**, 996 (2018).
12. L. van Biert, M. Godjevac, K. Visser, and P. V. Aravind, "Dynamic modelling of a direct internal reforming solid oxide fuel cell stack based on single cell experiments." *Appl. Energy*, **250**, 976 (2019).
13. Z. Xia, Z. Deng, D.-Q. Zhao, Y.-W. Xu, G.-Q. Liu, and J. Peng, "Modeling and analysis of cross-flow solid oxide electrolysis cell with oxygen electrode/electrolyte interface oxygen pressure characteristic for hydrogen production." *SSRN*, **529**, 231248 (2021).
14. M. Ni, "2D thermal modeling of a solid oxide electrolyzer cell (SOEC) for syngas production by H_2O/CO_2 co-electrolysis." *Int. J. Hydrogen Energy*, **37**, 6389 (2012).
15. M. Tomberg, M. P. Heddrich, S. A. Ansar, and K. A. Friedrich, "Operation strategies for a flexible megawatt scale electrolysis system for synthesis gas and hydrogen production with direct air capture of carbon dioxide." *Sustainable Energy & Fuels*, **7**, 471 (2023).
16. C. M. Stoots, J. E. O'Brien, K. G. Condie, and J. J. Hartvigsen, "High-temperature electrolysis for large-scale hydrogen production from nuclear energy—Experimental investigations." *Int. J. Hydrogen Energy*, **35**, 4861 (2010).
17. J. Aicart, J. Laurencin, M. Petitjean, and L. Dessemond, "Experimental validation of two-dimensional H_2O and CO_2 co-electrolysis modeling." *Fuel Cells*, **14**, 430 (2014).
18. W. G. Bessler, S. Gewies, and M. Vogler, "A new framework for physically based modeling of solid oxide fuel cells." *Electrochim. Acta*, **53**, 1782 (2007).
19. S. Srikanth, M. P. Heddrich, S. Gupta, and K. A. Friedrich, "Transient reversible solid oxide cell reactor operation—experimentally validated modeling and analysis." *Appl. Energy*, **232**, 473 (2018).
20. *Modelica Programming Language* (2023), [Online]. Available https://modelica.org/.
21. S. E. Mattsson and H. Elmqvist, "Modelica - an international effort to design the next generation modeling language." *IFAC Proceedings Volumes*, **30**, 151 (1997).
22. (Accessed 12.07.2024), [Online]. Available.
23. M. Tomberg, M. Heddrich, F. Sedeqi, D. Ullmer, A. Ansar, and K. Friedrich, "A new approach to modeling solid oxide cell reactors with multiple stacks for process system simulation." *J. Electrochem. Soc.*, **169**, 054530 (2022).
24. R. Chhabra and V. Shankar, "Chapter 6 - transport processes in microfluidic applications." *Coulson and Richardson's Chemical Engineering*, ed. R. Chhabra and V. Shankar (Butterworth-Heinemann, Oxford, United Kingdom) 7th ed.529 (2018).
25. P. Aguiar, C. S. Adjiman, and N. P. Brandon, "Anode-supported intermediate temperature direct internal reforming solid oxide fuel cell. I: model-based steady-state performance." *J. Power Sources*, **138**, 120 (2004).
26. A. Salogni and P. Colonna, "Modeling of solid oxide fuel cells for dynamic simulations of integrated systems." *Appl. Therm. Eng.*, **30**, 464 (2010).
27. A. Bejan, *Convection Heat Transfer* (John Wiley & Sons, Inc, Hoboken, NJ, USA) 4th ed. (2013), (Convection Heat Transfer).
28. J. P. Stempien, Q. Liu, M. Ni, Q. Sun, and S. H. Chan, "Physical principles for the calculation of equilibrium potential for co-electrolysis of steam and carbon dioxide in a solid oxide electrolyzer cell (SOEC)." *Electrochim. Acta*, **147**, 490 (2014).
29. M. Riedel, M. P. Heddrich, A. Ansar, Q. Fang, L. Blum, and K. A. Friedrich, "Pressurized operation of solid oxide electrolysis stacks: an experimental comparison of the performance of 10-layer stacks with fuel electrode and electrolyte supported cell concepts." *J. Power Sources*, **475**, 228682 (2020).
30. A. Leonide, Y. Apel, and E. Ivers-Tiffee, "SOFC modeling and parameter identification by means of impedance spectroscopy." *ECS Trans.*, **19**, 81 (2009).
31. H. Schichlein, A. C. Müller, M. Voigts, A. Krügel, and E. Ivers-Tiffée, "Deconvolution of electrochemical impedance spectra for the identification of electrode reaction mechanisms in solid oxide fuel cells." *J. Appl. Electrochem.*, **32**, 875 (2002).
32. A. Leonide, V. Sonn, A. Weber, and E. Ivers-Tiffée, "Evaluation and modeling of the cell resistance in anode-supported solid oxide fuel cells." *J. Electrochem. Soc.*, **155**, B36 (2007), /11/07 2008.
33. M. Riegraf, R. Costa, G. Schiller, K. A. Friedrich, S. Dierickx, and A. Weber, "Electrochemical impedance analysis of symmetrical Ni/Gadolinium-Doped Ceria (CGO10) electrodes in electrolyte-supported solid oxide cells." *J. Electrochem. Soc.*, **166**, F865 (2019).
34. M. Riedel, "Experimental analysis of the influence of elevated operating pressures on solid oxide cell stacks during steam, co- and CO2 electrolysis." *PhD thesis*, University of Stuttgart (2022), [Online]. Available, https://doi.org/10.18419/opus-1214810.18419/opus-12148.
35. C. Grosselindemann, F. Kullmann, T. Lehnert, O. Fritz, F. M. Fuchs, and A. Weber, "Comparison of a solid oxide cell with nickel/gadolinium-doped ceria fuel electrode during operation with hydrogen/steam and carbon monoxide/carbon dioxide." *Fuel Cells*, **23**, 442 (2023).
36. C. Grosselindemann, N. Russner, S. Dierickx, F. Wankmüller, and A. Weber, "Deconvolution of gas diffusion polarization in Ni/Gadolinium-doped ceria fuel electrodes." *J. Electrochem. Soc.*, **168**, 124506 (2021).
37. S. Santhanam, A. Padinjarethil, M. Tomberg, M. P. Heddrich, and A. Ansar, "Transient operation strategies for MW-Scale SOC systems." *ECS Trans.*, **91**, 2571 (2019).
38. Y. Fu et al., "Multicomponent gas diffusion in porous electrodes." *J. Electrochem. Soc.*, **162**, F613 (2015).
39. D. Bhattacharyya and R. Rengaswamy, "A review of solid oxide fuel cell (SOFC) dynamic models." *Ind. Eng. Chem. Res.*, **48**, 6068 (2009).
40. Wolfram, (2013), Binary Diffusion Coefficients for Gases. [Online]. Available: https://demonstrations.wolfram.com/BinaryDiffusionCoefficientsForGases/.
41. A. Zekri, M. Knipper, J. Parisi, and T. Plaggenborg, "Microstructure degradation of Ni/CGO anodes for solid oxide fuel cells after long operation time using 3D reconstructions by FIB tomography." *Phys. Chem. Chem. Phys.*, **19**, 13767 (2017).
42. M. Gross, F. Sedeqi, D.-M. Amaya-Dueñas, M. P. Heddrich, and S. A. Ansar, "Characterisation of a 10-Layer SOC stack under pressurised CO2 electrolysis operation." *ECS Meeting Abstracts*, **MA2022-02**, 1950 (2022).

43. M. Riegraf, D. M. Amaya-Duenas, N. Sata, K. A. Friedrich, and R. Costa, "Performance and limitations of nickel-doped chromite anodes in electrolyte-supported solid oxide fuel cells." *ChemSusChem*, **14**, 2401 (2021).

44. W. C. Chueh, Y. Hao, W. Jung, and S. M. Haile, "High electrochemical activity of the oxide phase in model ceria-Pt and ceria-Ni composite anodes." *Nat. Mater.*, **11**, 155 (2011).

45. M. Riegraf, M. P. Hoerlein, R. Costa, G. Schiller, and K. A. Friedrich, "Sulfur poisoning of electrochemical reformate conversion on nickel/gadolinium-doped ceria electrodes." *ACS Catal.*, **7**, 7760 (2017).

46. T. L. Skafte et al., "Selective high-temperature CO_2 electrolysis enabled by oxidized carbon intermediates." *Nat. Energy*, **4**, 846 (2019).

47. D. Chen, D. K. Niakolas, V. Papaefthimiou, E. Ioannidou, S. G. Neophytides, and S. Zafeiratos, "How the surface state of nickel/gadolinium-doped ceria cathodes influences the electrochemical performance in direct CO_2 electrolysis." *J. Catal.*, **404**, 518 (2021).

48. M. Riegraf, K. Develos-Bagarinao, I. Biswas, and R. Costa, "The influence of sulfur impurities in industrial CO_x gases on solid oxide electrolysis cell (SOEC) degradation." *J. Power Sources*, **559**, 232669 (2023).